Glomerular Barrier Behaves As an Atomically Precise Bandpass Filter in a Sub-nanometer Regime

Bujie Du[1], **Xingya Jiang**[1], **Anindita Das**[2], **Qinhan Zhou**[1], **Mengxiao Yu**[1], **Rongchao Jin**[2], and **Jie Zheng**[1,*]

[1]Department of Chemistry and Biochemistry, The University of Texas at Dallas, 800 West Campbell Road, Richardson, Texas 75080, USA

[2]Deparment of Chemistry, Carnegie Mellon University, Pittsburgh, Pennsylvania 15213, USA

Abstract

The glomerular filtration barrier is known as a "size cut-off" slit to retain nanoparticles or proteins larger than 6~8 nm in the body, and to rapidly excrete the smaller ones through the kidneys. However, in a sub-nm size regime, we found that this barrier behaved as an atomically precise "bandpass" filter to significantly slow down renal clearance of few-atom gold nanoclusters (AuNCs) with the same surface ligands but different sizes (Au_{18}, Au_{15} and Au_{10-11}). Compared to Au_{25} (~1.0 nm), just few-atom decreases in the size resulted in 4~9 times reductions in the renal clearance efficiency in the early elimination stage because the smaller AuNCs were more readily trapped by the glomerular glycocalyx than the larger ones. This unique *in vivo* nano-bio interaction in the sub-nm regime also slows down the extravasation of sub-nm AuNCs from normal blood vessels and enhances their passive targeting to cancerous tissues through enhanced permeability and retention effect. This discovery highlights the size precision in the body's response to nanoparticles and opens a new pathway to develop nanomedicines for many diseases associated with glycocalyx dysfunction.

Among many factors involved in the retention and elimination of engineered nanoparticles (NPs)[1–3], the size is known to play a key role[4–6]. Upon the particle size, engineered NPs interact with a variety of physiological barriers differently, are retained in the body for different periods of time and follow distinct clearance pathways[7–10]. For example, engineered NPs can end up in the spleen if their sizes are comparable to inter-endothelial cell slits of the spleen (200~500 nm)[9] or accumulate in the liver once their sizes are close to vascular fenestration of the liver (50~100 nm)[9]. This reticuloendothelial system (RES) (liver, spleen, etc.) uptake is the most common pathway for the body to remove engineered NPs with sizes above 6 nm out of blood stream, but it often takes much longer time for the body to completely eliminate them if they are not biodegradable[11]. On the other hand, for

*jiezheng@utdallas.edu.

engineered NPs with sizes below 6 nm, they can be readily eliminated through the kidneys by crossing a unique multiple-layer structure of glomeruli[12, 13]. For instance, Choi et al. developed a class of zwitterionic quantum dots (Qdots) and found that Qdots with hydrodynamic diameters (HDs) below 6 nm cleared out of the body through the urinary system much more efficiently than the larger ones: the renal clearance efficiency of Qdots increased from 45 %ID to 75 %ID (4 h post injection) with a just slight decrease of HDs from 5.64 nm to 4.64 nm[14]. A similar trend was also observed in renal clearable silica NPs[15]: a decrease of HD from 6 nm to 3.3 nm resulted in a significant increase of renal clearance efficiency from 55 %ID to 67.5 %ID (24 h post injection). We also developed renal clearable (AuNPs) with HDs of 3.0 nm[16] and 2.2 nm[17], which were eliminated out of the body at an efficiency of 43 and 53 %ID (24 h post injection), respectively. These studies are also consistent with a general observation of protein filtration through the glomeruli, where the smaller proteins such as 5.3 nm ScFv can be eliminated out of the body at an efficiency 7 times higher than those larger ones[14]. Moreover, the smaller 3.0 nm inulin is nearly 30% more efficient than 3.4 nm myoglobin in renal clearance[14]. With these findings, it has been generally accepted that the glomeruli serve as a one-directional "size cut-off" slit, where engineered NPs or proteins with the sizes smaller than 6 nm can pass through the kidneys and the smaller ones more efficiently clear out of the body than the larger ones.

Since size-dependent glomerular filtration is mainly observed from engineered NPs or proteins with sizes ranging from 2 nm to 6 nm. A fundamental question emerges: is this size-dependency in the glomerular filtration still valid at an even smaller size scale? Investigation of how the glomeruli filtrate out engineered NPs in the sub-nanometer (sub-nm) regime not only helps gain more comprehensive understandings of the glomerular filtration and kidney diseases in general but is also fundamental importance of precise control of nanomedicines that can break into much smaller fragments *in vivo*. Here, we reported that in a sub-nm size range (~1 nm), the glomerulus is no longer a "size cut-off" slit[18] but can become an atomically precise "bandpass" barrier to significantly slow down renal clearance of sub-nm gold nanoclusters (sub-nm AuNCs). In the sub-nm regime, renal clearance of AuNCs exponentially increases with an increase of the number of atoms in the particle. Unlike the size-dependency observed in the glomerular filtration of engineered NPs larger than 2 nm, which was mainly dictated by the pore size of glomerular basement membrane (GBM) and podocyte[19], the inverse size-dependency in the glomerular filtration in the sub-nm regime originated from a discovery that the smaller sub-nm AuNPs are more easily and physically retained by the endothelial glycocalyx of the glomerulus

Atomically precise glutathione-coated gold nanoclusters

The observation of size-dependency in the glomerular filtration in the sub-nm size regime was made possible by a recent breakthrough in the precise control of the number of gold atoms in sub-nm AuNCs[20–23]. Atomically precise AuNCs coated with glutathione (GSH) were synthesized by controlling reduction kinetics of gold ions in the presence of glutathione in aqueous solutions based on reported method [24] (Detailed procedures were described in supplementary information (SI) and specific literatures from ref 24 were cited in SI). Electrospray synthesis of $Au_{25}SG_{18}$, $Au_{18}SG_{14}$, $Au_{15}SG_{13}$ and $Au_{10-11}SG_{10-11}$ (Supplementary Fig. 1). While these AuNCs are slightly different in the numbers of

glutathione ligands on the particles, our recent studies have shown a 50% difference in the number of glutathione ligands on 2.5 nm AuNPs have little effect on their renal clearance efficiencies[25]. Moreover, a pharmacokinetics study of $Au_{22}SG_{18}$ and $Au_{22}SG_{16}$ further shows that a slight difference in the number of GS ligand induces little differences in blood retention and clearance of sub-nm AuNCs (Supplementary Fig. 2 and 3). All these results are consistent with the previous observation of renal clearance of a class of cysteine coated Qdots, where their sizes rather than the number of cysteine ligands govern their renal clearance efficiencies[14]. We specifically used glutathione to stabilize ultrasmall AuNCs because zwitterionic glutathione can effectively minimize adsorption of the AuNPs to serum protein [17, 26]. Similarly, these ultrasmall glutathione coated AuNCs are also highly resistant to the adsorption of serum protein and blood cells (Supplementary Fig. 4 and 5); thus they can retain their original sizes in native physiological environment and allow us to quantitatively correlate renal clearance, pharmacokinetics as well as tumour targeting with their original sizes without interference from serum protein and blood cells during the circulation. In addition, among these ultrasmall clusters, Au_{25} and Au_{18} give near-infrared (NIR) emissions (Supplementary Fig. 6), which allows us to in-situ fluorescently image the interactions of Au_{25} and Au_{18} with the endothelium of normal blood vessels.

Renal clearance of gold nanoclusters

Strong X-ray absorption cross section of gold atom offers a unique opportunity to noninvasively image renal clearance of these ultrasmall AuNCs. We selected three AuNCs, Au_{10-11}, Au_{18} and Au_{25}, with a 7-atom difference in size, for X-ray imaging studies. As shown in Supplementary Movie 1, Au_{25} was rapidly eliminated through the kidneys, renal elimination of Au_{18} was slow and renal clearance of Au_{10-11} was even slower. At 40 min post injection (p.i.), much more Au_{10-11} and Au_{18} were retained in the kidneys than Au_{25} (Fig. 1a) and the ratio of bladder to kidney derived from X-ray imaging was 2.32±0.25, 1.87±0.46 and 1.06±0.30 for Au_{25}, Au_{18} and Au_{10-11} (Fig. 1b), respectively. Since these AuNCs are highly physiologically stable and resistant to serum protein adsorption for both short (30 min.) and long period (24 hrs) (Supplementary Fig. 4 and 7), the observed differences in bladder/kidney ratios clearly indicate that the kidney filtration is highly sensitive to the cluster size in the sub-nm regime. In order to more quantitatively understand renal clearance of these atomically precise AuNCs, BALB/C mice were intravenously injected with 100 μL phosphate buffered saline (PBS) containing Au_{25}, Au_{18}, Au_{15} and Au_{10-11}, respectively at the same molar concentration of 100 μmol/L, followed by quantification of the Au amount in urine with inductively coupled plasma-mass spectrometry (ICP-MS) at 2, 5, 8, 12 and 24 h post injection (p.i.). Consistent with X-ray imaging studies, renal clearance of sub-nm AuNCs was highly sensitive to the number of Au atoms (Fig. 1c, Supplementary Table 2). A significant differences in renal clearance between Au_{25} (46.71 %ID, 2 h p.i.) to Au_{18} (to 10.79 %ID, 2 h p.i.) indicates that a 7-Au atom decrease in size can lead to a 4 times decrease in renal clearance efficiency at 2 h p.i.. Furthermore, the renal clearance efficiency declined to 6.03 and 5.29 %ID at 2 h p.i. once the cluster size was further reduced to Au_{15} and Au_{10-11}, respectively. At 24 h p.i., the urinary excretion of these AuNCs also decreased as the decrease of the number of Au atoms in the clusters (51.57, 26.82, 22.90 and 19.07 %ID for Au_{25}, Au_{18}, Au_{15} and Au_{10-11}, respectively). Comparing

those results with our previously reported renal clearance efficiencies of ~1.7 nm[17], ~2.5 nm[16] and ~6 nm GS-AuNPs[17](Fig. 1d), we found that Au_{25} (~1.0 nm) was almost identical to ~1.7 nm GS-AuNPs (Au_{201})[17] in renal clearance efficiency 24 hr p.i. (~52 %ID for Au_{25} and 53 %ID for 1.7 nm AuNPs), despite there is an 8-time difference in the number of Au atoms. But ~2.5 nm GS-AuNPs[16] (Au_{640}, ~43 %ID, 24 hr p.i.) cleared out of the body slowly than the smaller Au_{25} and Au_{201}. In addition, only 4 %ID of ~6 nm GS-AuNPs[17] (Au_{8856}, 24 hr p.i.) were renally cleared. Combining these results clearly shows an inverse size-dependency in renal clearance of AuNCs in the sub-nm region, distinct from the prevailing understanding that the smaller NPs always more rapidly clear through the urinary system than larger NPs [14, 15]. This indicates that the glomerulus (Fig. 1e), composed of glycocalyx, endothelial cells, glomerular basement membrane and podocyte,[12, 27] is no longer a one-directional "size-cut-off" slit[18] but becomes an atomically precise "bandpass" barrier to significantly slow down renal clearance of ultrasmall AuNPs with sizes in sub-nm regime (Fig. 1d).

Glomerular filtration of Au_{18} and Au_{25}

Since renal clearance is fundamentally governed by the glomerular filtration barrier, in order to unravel the origin of the observed size-dependent clearance in sub-nm regime, we investigated interactions of two representative AuNCs, Au_{18} and Au_{25}, with the glomeruli using electron microscope (EM) because these two AuNCs only have a 7-atom difference in size but exhibit a 4-time difference in renal clearance 2 hr p.i.. Since these AuNCs were too small to be directly revealed with EM, we applied silver staining[28] to increase their sizes and contrast. As shown in Supplementary Fig. 8, both Au_{18} and Au_{25} can catalyse the deposition of metallic silver on their surface, resulting in formation of larger hybrid silver-gold NPs in the glomerular arterioles and peritubular capillaries (yellow line) while no silver NPs were observed from the silver-stained glomerular tissues of the mouse without injection of AuNCs (Control). To unravel the differences of the nano-bio interactions between Au_{18} and Au_{25} *in vivo,* and avoid the interference from the AuNCs in the blood, we perfused the glomeruli with saline to remove those clusters that have weak interactions with the glomeruli in the blood, followed by tissue fixation with 4% paraformaldehyde/PBS. As shown in Fig. 2, all the fine structures of the glomeruli were observed, including endothelium (endothelial glycocalyx and endothelial cell), glomerular basement membrane, podocytes and glycocalyx layers. While no any silver NPs were observed from the control glomeruli after silver staining (Fig. 2a) and only few large silver-enhanced Au_{25} were found in the glomeruli of the mice injected with Au_{25} (Fig. 2b), a large number of monodispersed silver-enhanced Au_{18} were retained on the glycocalyx of endothelium and podocytes (Fig. 2c and Supplementary Fig. 9).

To unravel whether the long retention of Au_{18} on the glycocalyx is involved in any chemical interactions or not, we incubated Au_{18} with heparan sulfate proteoglycan, a major component of the glycocalyx layer[12, 29] for more than 24 hrs. As control, Au_{25} clusters were also investigated under the same condition. As shown in Supplementary Fig. 10, very little binding of Au_{18} and Au_{25} to heparan sulfate proteoglycan were observed, implying that the retention of smaller Au_{18} on the glycocalyx was not due to any specific chemical interactions. In addition, very few Au_{18} and Au_{25} were found in the glomeruli 7 days p.i. at

the tissue-level (Supplementary Fig. 11), further suggesting that both clusters were eventually filtered through the glomerular compartments without involvement of any specific cellular uptake. Therefore, the slow renal clearance of Au_{18} over Au_{25} is very likely because Au_{18} was physically retained on the glycocalyx for a longer period than Au_{25}, very similar to the inverse size-dependency observed in gel filtration or size-exclusion chromatography[30]: larger molecules/particles will be filtrated faster than smaller ones because the smaller ones are physically retained by stationary materials for a longer period. (Fig. 2d). These results also imply that potential pore sizes on the glycocalyx can be smaller than 1nm; as a result, they can retain sub-nm AuNCs for long periods of time.

Normal vessel extravasation and pharmacokinetics

As a major component of the glomerulus, the glycocalyx also lines normal blood vessels[31, 32]; thus, the long retention of Au_{18} on the endothelial glycocalyx observed in the glomeruli might also affect their extravasation from the normal blood vessels. By taking advantages of NIR emission from both Au_{18} and Au_{25}, we noninvasively imaged the extravasation of these two AuNCs from normal blood vessels to the interstitial tissue space in ears. As shown in Fig. 3a and Supplementary Movie 2 and 3, right after the intravenous injection, both of Au_{18} and Au_{25} were immediately transported to the artery, followed by a gradual increase in fluorescence intensities of the tissue interstitial space. We used the ratio of (interstitial intensity-background intensity) / (artery intensity-background intensity) to quantify the differences in extravasation between these two different AuNCs (Au_{18} and Au_{25}). As shown in Fig. 3b, it took 2.7 min for Au_{25} to reach an equivalent intensity between the tissue interstitial space and artery while the intensity of Au_{18} in the tissue interstitial space is only 37% of that in artery during the same period. This difference clearly indicates that it is more difficult for Au_{18} to cross the blood vessel walls than Au_{25} (Fig. 3c), consistent with the observation of the slow glomerular filtration of Au_{18} over Au_{25}.

While other smaller sized AuNCs are not luminescent and their interactions with the blood vessels were hardly imaged with fluorescence microscope like Au_{18} and Au_{25}, combination of the observed size-dependent renal clearance and the slow extravasation of smaller Au_{18} imply that other smaller AuNCs might also have longer blood retention and elimination half-lives. By quantifying their blood pharmacokinetics (Fig. 3d, Supplementary Table 3), we were able to obtain more quantitative nano-bio interactions *in vivo* in this sub-nm regime. As shown in Fig. 3d, the smallest Au_{10-11} exhibited the longest blood retention, followed by Au_{15}, Au_{18} and Au_{25}. At 2 min. p.i., the blood concentration of AuNCs linearly decreased from 28.45, to 25.51, 19.37, 12.13 %ID/g while the volume of distribution (Vd[33], a parameter that reflects the extent of NPs in extravascular tissues) linearly increased from 3.30 to 3.84, 4.55 and 6.07 mL with the number of atoms increased from 11 to 15, 18 to 25, respectively (Fig. 3e, Supplementary Table 4), consistent with the different extravasation kinetics of Au_{18} and Au_{25} from the fluorescence imaging studies. On the other hand, clearance (CL)[33], a parameter to measure the efficiency of the body in eliminating the particles through the urinary system, exponentially increased from 0.41, 0.50, 0.71 to 2.04 mL/h and the elimination half-life ($t_{1/2\beta}$) of AuNCs exponentially decreased from 5.65, 5.31, 4.47 to 2.09 hr with an increase of the number of atoms from 11, 15, 18 to 25, respectively (Fig. 3f, Supplementary Table 4). Consistency among these studies of the urine excretion,

glycocalyx retention, extravasation and pharmacokinetics of these sub-nm AuNCs clearly points out that *in vivo* behaviours of sub-nm AuNCs are highly size-dependent: the smaller sized AuNCs have longer the blood retention and slower extravasation and glomerular filtration.

Passive tumour targeting of gold nanoclusters

Not limited to glomerular filtration and extravasation from normal tissues, the passive tumour targeting of sub-nm AuNCs is also size-dependent. Using the nude mice bearing MCF-7 breast xenografts as model, we quantified the tumour targeting efficiencies of these AuNCs 24 h p.i., which were 8.17 ± 0.23 %ID/g, 6.07 ± 1.18 %ID/g, 5.27 ± 0.23 %ID/g and 2.28 ± 0.13 %ID/g, for Au_{10-11}, Au_{15}, Au_{18} and Au_{25}, respectively (Fig. 4a, other organs accumulation in Supplementary Fig. 12). These results clearly indicate that the efficiency of passive tumour targeting in the sub-nm regime linearly decreased with the increase of the number of Au atoms in the clusters. Once the sizes of AuNPs became larger than Au_{25}, this linear relationship vanished; instead, the tumour uptake of ~1.7 nm GS-AuNPs (Au_{201}, ~1.97 %ID/g) and ~2.5 nm GS-AuNPs (Au_{640}, ~2.00 %ID/g) became comparable to that of Au_{25} (2.28 %ID/g). To unravel the origin of the observed size-dependent tumour targeting of sub-nm AuNCs, we correlated tumour targeting efficiency with blood retention (area under pharmacokinetics curve, AUC). The linear relationship between the targeting efficiency and AUC (Fig. 4b) indicates that the size-dependent tumour targeting in the sub-nm regime is fundamentally due to size-dependent blood retention of sub-nm AuNCs: the smallest AuNCs, Au_{10-11}, has the longest retention in the blood; as a result, they have the highest accumulation in tumours. Since tumour/blood ratios of all the sub-nm AuNCs are all larger than 1 and much higher than muscle/blood ratios at 24 hr p.i. (Fig. 4c), the selective accumulation of sub-nm AuNCs is fundamentally because of the enhanced permeability and retention (EPR) effect[34]: leaky and dense vasculature leading to long-retention of nano sized particles in tumours. Further investigation of distribution of Au_{18} and Au_{25} in tumours 24 hr p.i. (Fig. 4d) confirms that both AuNCs crossed the leaky tumour vasculature and entered tumour microenvironment. More importantly, because Au_{18} has much longer blood retention than Au_{25}, more Au_{18} clusters were retained in tumour microenvironment than Au_{25} clusters, consistent with the observed size-dependent tumour targeting in the sub-nm regime. Combination of these results with our previous observation of passive tumour targeting of 2.5 nm renal clearable AuNPs[26, 35] confirms that the EPR effect is indeed retained in renal clearable AuNPs with size down to few atoms, which could further broaden EPR effect, a major strategy used by large non-renal clearable NPs in the tumour targeting[5].

Different from tumour/blood ratios, the ratios of the liver, spleen and intestine to the blood at 24 hrs. p.i. were all close to 1 (Fig. 4e), suggesting that these ultrasmall AuNCs have little interactions with those RES organs. On the other hand, the ratio of the kidney to the blood was much larger than 1 (Fig. 4e) and the kidney accumulation of these AuNCs continually decreased over time (Supplementary Fig. 13), clearly indicating that the kidneys remain the major organ for eliminating these ultrasmall AuNCs. After one month, the major organs accumulation of different-sized AuNCs decreased to 1.5 %ID (Fig. 4f, Supplementary Fig. 14), suggesting that all these AuNCs were gradually eliminated from the body through the urinary system.

In summary, by investigating *in vivo* behaviours of sub-nm AuNCs with high resistance to the binding of serum protein and blood cells, we discovered that the glomeruli can serve as an atomically precise barrier to slow down the renal clearance of the clusters with size below 1 nm: a few-atom decrease in the cluster size results in a nearly one order reduction in renal clearance. This "surprising" observation fundamentally originates from the fact that the smaller AuNCs are more easily and physically retained by the glycocalyx of the glomeruli, similar to the separation principle used in gel filtration or size-exclusion chromatography. Such size-dependent interaction between sub-nm AuNCs and the glycocalyx also dictates the extravasation of sub-nm AuNCs from normal blood vessels and significantly impacts their accumulation in cancerous tissues through EPR effect. This discovery highlights how precisely the glomerulus and the body could response to ultrasmall AuNPs, which might be generalized to many other renal clearable nanosystems[14, 15, 36] and further improve our comprehensive understandings of the glomerular filtration in the sub-nm regime. Considering the similarity of rodents and human in the pore sizes of glomerular filtration membrane (Supplementary Table S1), these findings will also open a new pathway to design clinically translatable precision nanomedicines that can target many endothelial-dysfunction associated diseases such as strokes, atherosclerosis, hypertension, chronic renal failure once the biocompatibility of these renal clearable smaller AuNCs is fully investigated.

Method

Materials and equipment

Hydrogen tetrachloroaurate used for the synthesis of gold nanoclusters was obtained from Fisher Scientific (U.S.). All the other chemicals were obtained from Sigma-Aldrich and used as received unless specified. The gold in urine, blood and each organ was detected by Agilent 7900 inductively coupled plasma mass spectrometry (ICP-MS). The luminescence spectra of $Au_{18}SG_{14}$, $Au_{25}SG_{18}$ and $Au_{22}SG_{16}$, $Au_{22}SG_{18}$ were collected with a PTI QuantaMaster™ 30 Fluorescence Spectrophotometer (Birmingham, NJ). The blood-vessel images were taken with IX-71 microscope (Olympus). Optical images of kidneys and tumours were taken with IX-71 microscope (Olympus). Electron microscopic (EM) images of the kidney were recorded with a 120 kV Tecnai G^2 spirit transmission electron microscope (FEI) equipped with a LaB_6 source. The animal studies were performed according to the guidelines of the University of Texas System Institutional Animal Care and Use Committee. The female BALB/c mice (BALB/cAnNCr, strain code is 047) of 6–8 weeks old, weighing 20~25 g, were purchased from Envigo. The female nude mice (Athymic NCr-nu/nu, strain code is 069) of 6–8 weeks old, weighing 20–25 g, were also purchased from Envigo for tumour targeting study. All of these mice were randomly allocated and four-group-housed per ventilated cage under standard environmental conditions (23±1°C, 50±5% humidity and a 12/12 h light/dark cycle) with free access to water and standard laboratory food.

Synthesis of glutathione-coated gold nanoclusters

The gold nanoclusters were synthesized according to previously reported procedures with slight modifications[37–42]. The $Au_{10-11}SG_{10-11}$ and $Au_{15}SG_{13}$ nanoclusters were synthesized using carbon monoxide (CO) as a reducing agent under a controlled pH condition.[37] Briefly,

aqueous solutions of $HAuCl_4 \cdot 3H_2O$ (6.25 mL, 20 mM) and glutathione (GSH, 5 mL, 50 mM) were added to 114 mL water. This reaction mixture was stirred vigorously for 2 minutes, followed by adjusting pH to 7 and 9 with 1 M sodium hydroxide for the synthesis of $Au_{10-11}SG_{10-11}$ and $Au_{15}SG_{13}$, respectively. CO gas was bubbled through the mixture at one atmospheric pressure to reduce Au(I)-SG for 3–4 minutes. The reaction flasks were then sealed and the solutions were stirred for 24 h at room temperature.

Synthesis of $Au_{18}SG_{14}$[38]: aqueous solutions of $HAuCl_4 \cdot 3H_2O$ (2 mL, 10 mM) and glutathione (3 mL, 20 mM) were added to 15 mL water and stirred vigorously for 5 minutes. Then, a solution of borane *tert*–butylamine in toluene (20 mL, 10 mM) was added to the above mixture and the reaction mixture was stirred overnight (~16 h). After completion of the reaction, the aqueous phase was concentrated under a reduced pressure, followed by precipitation of the crude cluster product with excess methanol. The as-obtained precipitate was washed repeatedly with methanol and finally dried under vacuum to yield $Au_{18}SG_{14}$ clusters in a powder form.

Synthesis of $Au_{25}SG_{18}$[39, 40]: In the first step, $HAuCl_4 \cdot 3H_2O$ (0.090 g, 0.228 mmol) was first dissolved in 5 mL water, then added to a toluene solution of tetraoctylammonium bromide (10 mL, 0.145 g, 0.265 mmol). The two-phase solution was vigorously stirred for 15 min for phase transfer of Au(III) salt from aqueous to toluene phase. The aqueous layer was then removed, and triphenylphosphine (PPh_3) (0.180 g, 0.686 mmol) was added under vigorous stirring. A freshly prepared ethanol solution of sodium borohydride ($NaBH_4$) (0.026 g, 0.684 mmol, 5 mL) was rapidly added to the whitish suspension to reduce Au(I)-$(PPh_3)_X$ (X=Cl or Br) to the clusters. After 6 h, toluene was removed via rotary evaporation. The resulting reddish brown product was first washed with water followed by repeated hexane:dichloromethane (6:1) washings to remove excess reactants. The Au:PPh_3 clusters were finally extracted with dichloromethane, to which an aqueous solution of GSH (5 mL, 0.400 g, 1.3 mmol) was added. This reaction was stirred at 55 °C for 36 h. Then excess acetone was added to the aqueous phase to precipitate out the crude $Au_{25}SG_{18}$ cluster product. The as-obtained precipitate was then repeatedly washed with excess methanol and dried under vacuum to yield $Au_{25}SG_{18}$ clusters in powder form.

Synthesis of $Au_{22}SG_{16}$ and $Au_{22}SG_{18}$[41, 42]: 1.0 mmol of glutathione was added to the methanol solution (50 mL) of $HAuCl_4$ (0.25 mmol). The mixture was cooled to 0°C for 30 min. The aqueous solution of $NaBH_4$ (0.2 M, 12.5 mL) was added into the mixture, after which this mixture was stirred at 1600 rpm for 60 min. The resulting precipitate was washed with methanol repeatedly and purified with NAP-5 column in water to remove the impurities. The as-synthesized Au nanoclusters were separated using polyacrylamide gel electrophoresis.

Stability test of the AuNCs in the physiological environment

To test whether these AuNCs bind to serum protein or not, the $Au_{10-11}SG_{10-11}$, $Au_{15}SG_{13}$, $Au_{18}SG_{14}$ and $Au_{25}SG_{18}$ were incubated with either phosphate-buffered saline (PBS) or PBS supplemented with 10% (v/v) fetal bovine serum (FBS) at 37 °C for 30 min. In addition, $Au_{10-11}SG_{10-11}$, $Au_{18}SG_{14}$ and $Au_{25}SG_{18}$ were incubated with PBS or PBS supplemented with 10% (v/v) FBS at 37 °C for 24 h to test whether these AuNCs bind to

serum protein after long-term (24 h) incubation with FBS. In order to identify the colorless protein band, FBS incubated-$Au_{10-11}SG_{10-11}$, $Au_{15}SG_{13}$, $Au_{18}SG_{14}$, $Au_{25}SG_{18}$ and pure FBS were stained by 10% (v/v) Coomassie Brilliant Blue 250 (CBB 250). All these samples were analyzed using 2% agarose gel electrophoresis (Mini-sub cell GT Gel electrophoresis system from Bio-Rad Laboratories INc.). The amount of gold in each band was quantified using ICP-MS.

To quantify the long-term physiological stability of these AuNCs, $Au_{10-11}SG_{10-11}$, $Au_{18}SG_{14}$ and $Au_{25}SG_{18}$ were incubated with PBS solution supplemented with 10% (v/v) FBS for 24 h incubation at 37 °C. Their UV-vis absorption spectra were collected at different incubation time points (0, 1, 12 and 24 h).

Blood-cell binding test

The whole blood was collected from female BALB/c mice (6–8 weeks, 20–25 g) and then stored in an anti-coagulation BD Vacutainer. This blood was divided into 4×3 groups for incubation with $Au_{10-11}SG_{10-11}$, $Au_{15}SG_{13}$, $Au_{18}SG_{14}$, $Au_{25}SG_{18}$ at a 10% v/v ratio at room temperature for 30 min, followed by being centrifuged at room temperature at 500g to separate the plasma and blood cells. Finally, the amounts of gold in plasma and blood cells were quantified using ICP-MS.

X-ray kidney images of the mice after intravenous injection of Au_{10-11}, Au_{18} and Au_{25}

All X-ray images of kidneys were taken using Bruker *In-vivo* Xtreme Imaging. Parameters: X-ray: 0.8 mm, KVP:45, Exposure type: standard, Mode: high speed, Exposure time: 15 sec, Bin: 1×1, FOV:12, fStop: 5.6, Focal plane: 0 mm. BALB/c mice were imaged under above parameters after intravenously injected with $Au_{10-11}SG_{10-11}$, $Au_{18}SG_{14}$ and $Au_{25}SG_{18}$ for 40 min. ($Au_{10-11}SG_{10-11}$: n=3; $Au_{18}SG_{14}$: n=4; $Au_{25}SG_{18}$: n=3)

In vivo renal clearance kinetics study

BALB/c mice were intravenously injected with $Au_{10-11}SG_{10-11}$ (n=3), $Au_{15}SG_{13}$ (n=3), $Au_{18}SG_{14}$ (n=6) and $Au_{25}SG_{18}$ (n=3), respectively (~100 μmol/L, 100 μL) and then placed in metabolism cages. Mouse urine was collected at 2 h, 5 h, 8 h, 12 h, and 24 h post injection. Then, the urine was completely lysed in freshly made aqua regia in plastic centrifuge tube (15 mL) for 2 days, then diluted to 10 mL using ultrapure water. All of above samples were centrifuged at 4500 rpm, 5 min and analyzed by ICP-MS.

Optical kidney images of the mice after injection of $Au_{18}SG_{14}$ and $Au_{25}SG_{18}$

$Au_{18}SG_{14}$ and $Au_{25}SG_{18}$ of 300 μL (~0.7 mmol/L) as well as 300 μL PBS (control) were iv injected into the mice, respectively. The mice were sacrificed at 10 min and 7 days p.i., and kidneys were then harvested and fixed by 4% formalin, followed by dehydration and paraffin embedding. The fixed kidneys were then sectioned into 4 μm slices. To image these ultrasmall gold clusters under bright-field optical microscopes, the silver staining was used to enhance their sizes and contrast. Before silver staining, these slices were dewaxed using xylene and then dried in lab oven at 65 °C. Each kidney slice was incubated in the silver staining solution containing 40 μL 0.1 M silver nitrate, 40 μL 0.2 g/L hydroquinone for 30 min. These silver-stained slices were then washed with ultrapure water and dried in lab oven

at 65 °C again. These final samples were imaged with an IX71 optical microscope in a bright-field mode.

Electron microscopic images of the glomerulus of the mice after intravenous injection of $Au_{18}SG_{14}$ and $Au_{25}SG_{18}$

Firstly, the mice were sacrificed and fixed via transcardial perfusion at 10-min time point after i.v. injection of $Au_{25}SG_{18}$ (~0.7 mmol/L, 300 μL), $Au_{18}SG_{14}$ (~0.7 mmol/L, 300 μL) and PBS (300 μL, control), respectively. Briefly, 10 mL heparizinzed normal saline as initial perfusant was used to remove the whole-body blood under the perfusion speed of 75 mL/h, then 10 mL 4% paraformaldehyde/PBS fixative as second perfusant was injected to fix the whole animals at the same perfusion speed. After fixation perfusion, the kidneys were collected and cut into pieces of 1 mm^3, which then were immersed in 4% paraformaldehyde/PBS in scintillation vials. Fixation was continued by immersion with agitation at 4 °C for 24–72 h. Secondly, these kidneys were then rinsed with 0.1 M sodium cacodylate buffer and post-fixed with 1% osmium tetroxide and 0.8 % potassium ferricyanide in 0.1 M sodium cacodylate buffer for one and a half hours at room temperature, followed by being rinsed with water and en bloc stained with 4% uranyl acetate in 50% ethanol for two hours. The kidney tissues were then dehydrated with increasing concentrations of ethanol, transitioned into resin with propylene oxide, infiltrated with Embed-812 resin and polymerized in a 60 °C oven overnight. Thirdly, the blocks were sectioned with a diamond knife (Diatome) on a Leica Ultracut 6 ultramicrotome (Leica Microsystems) and collected onto grids, followed by the silver-staining with the same method described above. Finally, EM images were taken using a Tecnai G^2 spirit transmission electron microscope.

Glycocalyx-binding test of $Au_{18}SG_{14}$ and $Au_{25}SG_{18}$

To test whether these AuNCs chemically bind to the glycocalyx, we incubated $Au_{18}SG_{14}$ and $Au_{25}SG_{18}$ with 10% (v/v) major component of glycocalyx-heparan sulfate (HS) proteoglycan from Sigma-Aldrich in PBS at 37 °C for 30 min and 24 h, respectively. In order to identify the colorless HS proteoglycan band, HS proteoglycan incubated-$Au_{18}SG_{14}$, $Au_{25}SG_{18}$ were stained by 10% (v/v) Coomassie brilliant blue 250 (CBB 250). All these samples were analyzed by 2% agarose gel electrophoresis using the Mini-sub cell GT Gel electrophoresis system (Bio-Rad Laboratories INc.). The amount of gold in each band was quantified using ICP-MS.

In-situ blood-vessel imaging

The BALB/c mice were placed on the imaging station of an IX-71 microscope (Olympus) under isoflurane anesthesia after the removal of ear hair. The bright field images of blood vessels in ear were taken with a 10 x objective and Photon Max 512 CCD camera (Princeton Instruments). After the breath rate of mice was controlled at ~16–20/min, these mice were injected with $Au_{18}SG_{14}$ (~0.7 mmol/L, 300μL) and $Au_{25}SG_{18}$ (~0.7 mmol/L, 300μL) through the tail vein respectively (n=3 for $Au_{18}SG_{14}$, n=3 for $Au_{25}SG_{18}$). The fluorescence images were taken with 10 x objective under Hg-lamp excitation (Ex: 480/40 nm; Em: 700 Lang Path; Dichroic mirror: 560 nm; Exposure time: 2 s) right after the injection.

Pharmacokinetics study

The BALB/c mice (n=3 for each nanocluster) were intravenously injected with $Au_{10-11}SG_{10-11}$, $Au_{15}SG_{13}$, $Au_{18}SG_{14}$ and $Au_{25}SG_{18}$, $Au_{22}SG_{16}$, $Au_{22}SG_{18}$ (~100 μmol/L, 100 μL), respectively, followed by collection of ~30 μL blood samples from retro-orbital at 2, 5, 10, 30 min, 1, 3, 5, 8, 12, and 24 h and 48 h p.i.. The blood samples were weighted and completely lysed in 1 mL freshly made aqua regia in screw capped glass bottles (10 mL) for 3 days. They were then diluted into 10 mL using ultrapure water and transferred into 15 mL plastic centrifuge tube, centrifuged at 4500 rpm for 5 min to remove insoluble components. The final samples were analyzed with ICP-MS.

Tumour-targeting efficiency study

Tumour implantation: The human breast cancer cell line MCF-7 (purchased from ATCC company) was cultured in Minimum Essential Medium (MEM) with 10% (v/v) fetal bovine serum (FBS) and 1% (v/v) penicillin-streptomycin at 37 °C in humidified atmosphere containing 5% CO_2. The cell suspension (in MEM with 10% (v/v) FBS) was then mixed 2:1 (v/v) with matrix gel and injected subcutaneously upper near the mammary fat pad (MFP) area of the nude mouse with a volume of 100 μL dense suspension (containing about 1×10^6 cells) for each mouse. The tumour was allowed to grow ~2 weeks and reach a ~6–8 mm size before the study. $Au_{10-11}SG_{10-11}$, $Au_{15}SG_{13}$, $Au_{18}SG_{14}$ and $Au_{25}SG_{18}$ (~100 μmol/L, 100 μL) were intravenously injected into MCF-7 tumour bearing nude mice (n=3), respectively. These tumours were collected and weighed after 24 h post injection. The amount of gold in the tumour tissues (% injection dose/g, % ID/g) were determined using ICP-MS.

Biodistribution study

To quantify the distributions of $Au_{10-11}SG_{10-11}$, $Au_{15}SG_{13}$, $Au_{18}SG_{14}$ and $Au_{25}SG_{18}$ in the tissues and organs over time, the mice were sacrificed 12 h p.i. (the whole blood was perfused before the mice sacrificed), 7 days and 1 month after intravenous injection of $Au_{10-11}SG_{10-11}$, $Au_{15}SG_{13}$, $Au_{18}SG_{14}$ and $Au_{25}SG_{18}$ (~100 μmol/L, 100 μL) respectively (n=3). Then major organs and tissues were collected and measured by ICP-MS to detect gold concentration (% injection dose/g, % ID/g).

Statistical analysis

Error bars are reported as mean ± s.d. The differences between groups were compared by analysis of Student's t-test and One-way ANOVA with the result shown in Fig. 4, Supplementary Fig. 3, Fig. 5. P-value <0.05 was considered to be statistically significant. ns (no significant), *P<0.05 (significant), **P<0.005 (highly significant). Investigators conducting the experiments were not blinded. Dixon's Q test is used for identification and rejection of outliers in data analysis.

Data availability

The data that support the plots within this paper and other findings of the study are available from the corresponding author upon reasonable request.

Supplementary Material

Refer to Web version on PubMed Central for supplementary material.

Acknowledgments

References

1. Ohta S, Glancy D, Chan WC. DNA-controlled dynamic colloidal nanoparticle systems for mediating cellular interaction. Science. 2016; 351:841–845. [PubMed: 26912892]

2. Shi J, Kantoff PW, Wooster R, Farokhzad OC. Cancer nanomedicine: progress, challenges and opportunities. Nature Reviews Cancer. 2016

3. Albanese A, Tang PS, Chan WC. The effect of nanoparticle size, shape, and surface chemistry on biological systems. Annual review of biomedical engineering. 2012; 14:1–16.

4. Chithrani BD, Ghazani AA, Chan WC. Determining the size and shape dependence of gold nanoparticle uptake into mammalian cells. Nano letters. 2006; 6:662–668. [PubMed: 16608261]

5. Sykes EA, Chen J, Zheng G, Chan WC. Investigating the impact of nanoparticle size on active and passive tumor targeting efficiency. ACS nano. 2014; 8:5696–5706. [PubMed: 24821383]

6. Huang K, et al. Size-Dependent Localization and Penetration of Ultrasmall Gold Nanoparticles in Cancer Cells, Multicellular Spheroids, and Tumors in Vivo. ACS Nano. 2012; 6:4483–4493. [PubMed: 22540892]

7. Wang B, He X, Zhang Z, Zhao Y, Feng W. Metabolism of nanomaterials in vivo: blood circulation and organ clearance. Accounts of chemical research. 2012; 46:761–769. [PubMed: 23964655]

8. Yu M, Zheng J. Clearance Pathways and Tumor Targeting of Imaging Nanoparticles. ACS nano. 2015

9. Blanco E, Shen H, Ferrari M. Principles of nanoparticle design for overcoming biological barriers to drug delivery. Nature biotechnology. 2015; 33:941–951.

10. Longmire M, Choyke PL, Kobayashi H. Clearance properties of nano-sized particles and molecules as imaging agents: considerations and caveats. 2008

11. Ye L, et al. A pilot study in non-human primates shows no adverse response to intravenous injection of quantum dots. Nature Nanotechnology. 2012; 7:453–458.

12. Haraldsson B, Nyström J, Deen WM. Properties of the glomerular barrier and mechanisms of proteinuria. Physiological reviews. 2008; 88:451–487. [PubMed: 18391170]

13. Hall, JE. Guyton and Hall textbook of medical physiology. Elsevier Health Sciences; 2015.

14. Choi HS, et al. Renal clearance of quantum dots. Nature biotechnology. 2007; 25:1165–1170.

15. Burns AA, et al. Fluorescent silica nanoparticles with efficient urinary excretion for nanomedicine. Nano letters. 2008; 9:442–448.

16. Zhou C, et al. Near - Infrared Emitting Radioactive Gold Nanoparticles with Molecular Pharmacokinetics. Angewandte Chemie. 2012; 124:10265–10269.

17. Zhou C, Long M, Qin Y, Sun X, Zheng J. Luminescent gold nanoparticles with efficient renal clearance. Angewandte Chemie. 2011; 123:3226–3230.

18. Venturoli D, Rippe B. Ficoll and dextran vs. globular proteins as probes for testing glomerular permselectivity: effects of molecular size, shape, charge, and deformability. American Journal of Physiology-Renal Physiology. 2005; 288:F605–F613. [PubMed: 15753324]

19. Rennke HG, Cotran RS, Venkatachalam MA. Role of molecular charge in glomerular permeability. Tracer studies with cationized ferritins. The Journal of cell biology. 1975; 67:638–646. [PubMed: 1202017]

20. Azubel M, et al. Electron microscopy of gold nanoparticles at atomic resolution. Science. 2014; 345:909–912. [PubMed: 25146285]

21. Li G, Jiang D-e, Kumar S, Chen Y, Jin R. Size Dependence of Atomically Precise Gold Nanoclusters in Chemoselective Hydrogenation and Active Site Structure. ACS Catalysis. 2014; 4:2463–2469.

22. Jadzinsky PD, Calero G, Ackerson CJ, Bushnell DA, Kornberg RD. Structure of a thiol monolayer-protected gold nanoparticle at 1.1 Å resolution. Science. 2007; 318:430–433. [PubMed: 17947577]

23. Zheng J, Petty JT, Dickson RM. High quantum yield blue emission from water-soluble Au8 nanodots. Journal of the American Chemical Society. 2003; 125:7780–7781. [PubMed: 12822978]

24. Jin R, Zeng C, Zhou M, Chen Y. Atomically Precise Colloidal Metal Nanoclusters and Nanoparticles: Fundamentals and Opportunities. Chemical Reviews. 2016; 116:10346–10413. [PubMed: 27585252]

25. Tang S, et al. Tailoring Renal Clearance and Tumor Targeting of Ultrasmall Metal Nanoparticles with Particle Density. Angewandte Chemie. 2016

26. Liu J, et al. Passive tumor targeting of renal-clearable luminescent gold nanoparticles: long tumor retention and fast normal tissue clearance. Journal of the American Chemical Society. 2013; 135:4978–4981. [PubMed: 23506476]

27. Singh A, Satchell SC. Microalbuminuria: causes and implications. Pediatric Nephrology. 2011; 26:1957–1965. [PubMed: 21301888]

28. Chou LY, Fischer HC, Perrault SD, Chan WC. Visualizing quantum dots in biological samples using silver staining. Analytical chemistry. 2009; 81:4560–4565. [PubMed: 19408951]

29. Vernier RL, Steffes MW, Sisson-Ross S, Mauer SM. Heparan sulfate proteoglycan in the glomerular basement membrane in type 1 diabetes mellitus. Kidney international. 1992; 41:1070–1080. [PubMed: 1513088]

30. Rubinson, KA., Rubinson, JF. Contemporary instrumental analysis. Prentice Hall; Upper Saddle River, NJ: 2000.

31. Uhl B, et al. The Endothelial Glycocalyx Controls Interactions of Quantum Dots with the Endothelium and Their Translocation Across the Blood-Tissue Border. ACS nano. 2017

32. Nieuwdorp M, et al. The endothelial glycocalyx: a potential barrier between health and vascular disease. Current opinion in lipidology. 2005; 16:507–511. [PubMed: 16148534]

33. Greenblatt DJ. Elimination half-life of drugs: value and limitations. Annual review of medicine. 1985; 36:421–427.

34. Fang J, Nakamura H, Maeda H. The EPR effect: unique features of tumor blood vessels for drug delivery, factors involved, and limitations and augmentation of the effect. Advanced drug delivery reviews. 2011; 63:136–151. [PubMed: 20441782]

35. Liu J, et al. PEGylation and Zwitterionization: Pros and Cons in the Renal Clearance and Tumor Targeting of Near - IR - Emitting Gold Nanoparticles. Angewandte Chemie. 2013; 125:12804–12808.

36. Kang H, et al. Renal Clearable Organic Nanocarriers for Bioimaging and Drug Delivery. Advanced Materials. 2016; 28:8162–8168. [PubMed: 27414255]

37. Yu Y, et al. Scalable and precise synthesis of thiolated Au10–12, Au15, Au18, and Au25 nanoclusters via pH controlled CO reduction. Chemistry of Materials. 2013; 25:946–952.

38. Yao Q, et al. Two - Phase Synthesis of Small Thiolate - Protected Au15 and Au18 Nanoclusters. Small. 2013; 9:2696–2701. [PubMed: 23447552]

39. Shichibu Y, Negishi Y, Tsukuda T, Teranishi T. Large-scale synthesis of thiolated Au25 clusters via ligand exchange reactions of phosphine-stabilized Au11 clusters. Journal of the American Chemical Society. 2005; 127:13464–13465. [PubMed: 16190687]

40. Das A, et al. Total structure and optical properties of a phosphine/thiolate-protected Au24 nanocluster. Journal of the American Chemical Society. 2012; 134:20286–20289. [PubMed: 23227995]

41. Negishi Y, Nobusada K, Tsukuda T. Glutathione-protected gold clusters revisited: Bridging the gap between gold (I)– thiolate complexes and thiolate-protected gold nanocrystals. Journal of the American Chemical Society. 2005; 127:5261–5270. [PubMed: 15810862]

42. Yu Y, et al. Identification of a highly luminescent Au22 (SG) 18 nanocluster. Journal of the American Chemical Society. 2014; 136:1246–1249. [PubMed: 24387227]
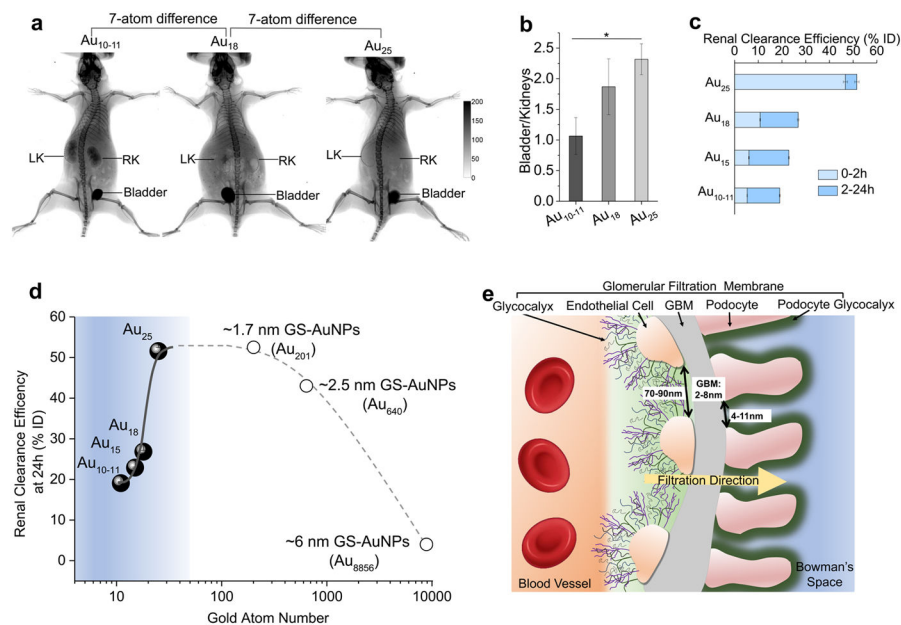
Figure 1. Renal clearance of different sized gold nanoclusters and schematic diagram of the glomerular filtration membrane

a, Whole-body X-ray images of the mice after being intravenously injected with Au_{10-11}, Au_{18} and Au_{25}, respectively at 40 min post injection. While all three different AuNCs were cleared through the kidneys into the bladder, the smallest Au_{10-11} has much longer kidney retention than Au_{18}, which in turn has longer kidney retention than Au_{25} even though there is only a 7-atom difference among these three AuNCs. **b**, The X-ray intensity bladder to kidney ratios of Au_{10-11}, Au_{18} and Au_{25} at 40 min post injection, clearly showing that more Au_{10-11} and Au_{18} were retained in the kidneys than Au_{25}. * means P<0.05 based on One-way ANOVA. (n=3 for Au_{10-11}, Au_{25}, n=4 for Au_{18}) **c,** Renal clearance efficiency of Au_{10-11}, Au_{15}, Au_{18} and Au_{25} in 0–2 h and 2–24 h after intravenous injection (n=3 for Au_{10-11}, Au_{15}, Au_{25}, n=6 for Au_{18}). **d**, The renal clearance efficiencies of Au_{10-11}, Au_{15}, Au_{18} and Au_{25}, 1.7 nm (Au_{201}), 2.5 nm (Au_{640}) and 6 nm (Au_{8856}) GS-AuNPs 24h post injection over the number of gold atoms. Below Au_{25}, the renal clearance efficiency exponentially decreased with the decrease of the number of gold atoms in the NPs. **e**, Glomerulus[12], an important component of renal filtration, is composed of kidney blood vessel, glomerular filtration membrane and Bowman's space. The glomerular filtration membrane is composed of multiple layers: endothelial glycocalyx, endothelial cell, glomerular basement membrane (GBM) and podocyte. Podocytes are covered by 200 nm glycocalyx. Generally, the fenestration between endothelial cells is 70–90 nm; GBM junction is 2–8 nm; the sizes of podocyte slits are in the range of 4–11 nm (These numbers are measured in rat kidney but very similar to those found in human kidneys, Supplementary Table 1). Combination of these layers, the size threshold for kidney filtration is ~6 nm: NPs or proteins with a hydrodynamic diameter (HD) <6 nm can pass through glomerular filtration membrane readily while it is difficult for the large ones to cross through it.
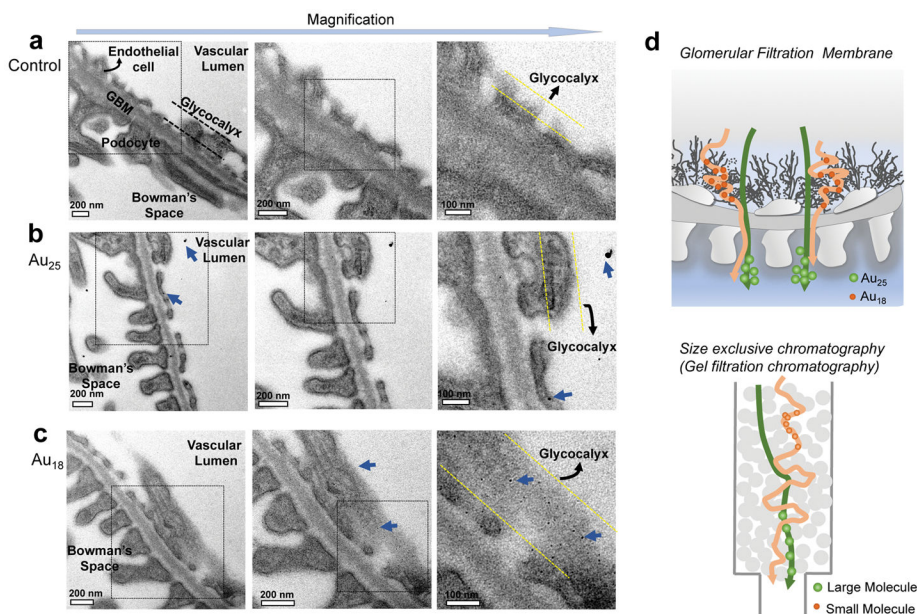
Figure 2. Electron microscopic images of ultrastructure of glomerular filtration membrane (GFM) from the mice after intravenous injection of PBS, Au$_{25}$ and Au$_{18}$, respectively
a, The GFM of the mouse injected with no particle, only PBS. No any NPs were observed from control glomeruli. **b,** The GFM of the mice at 10 min post injection of Au$_{25}$, only few large silver-enhanced Au$_{25}$ were found in the glomeruli of the mouse. **c,** The GFM of the mouse at 10 min post injection of Au$_{18}$, a large number of monodispersed silver-enhanced Au$_{18}$ were observed, which mainly bound to the glycocalyx of endothelial cells, glomerular basement membrane (GBM) as well as podocytes. **d**, Comparison between the glomerular filtration of these sub-nm AuNCs and size exclusive/gel filtration chromatography. Au$_{18}$ was more easily retained by the glycocalyx than Au$_{25}$, as a result, Au$_{25}$ was filtrated much faster than Au$_{18}$ during the same time of period, very similar to the separation in the size exclusive/gel filtration chromatography, where larger molecules/particles will be filtrated faster than smaller ones because the smaller ones are physically retained by the stationary phase for a longer period.
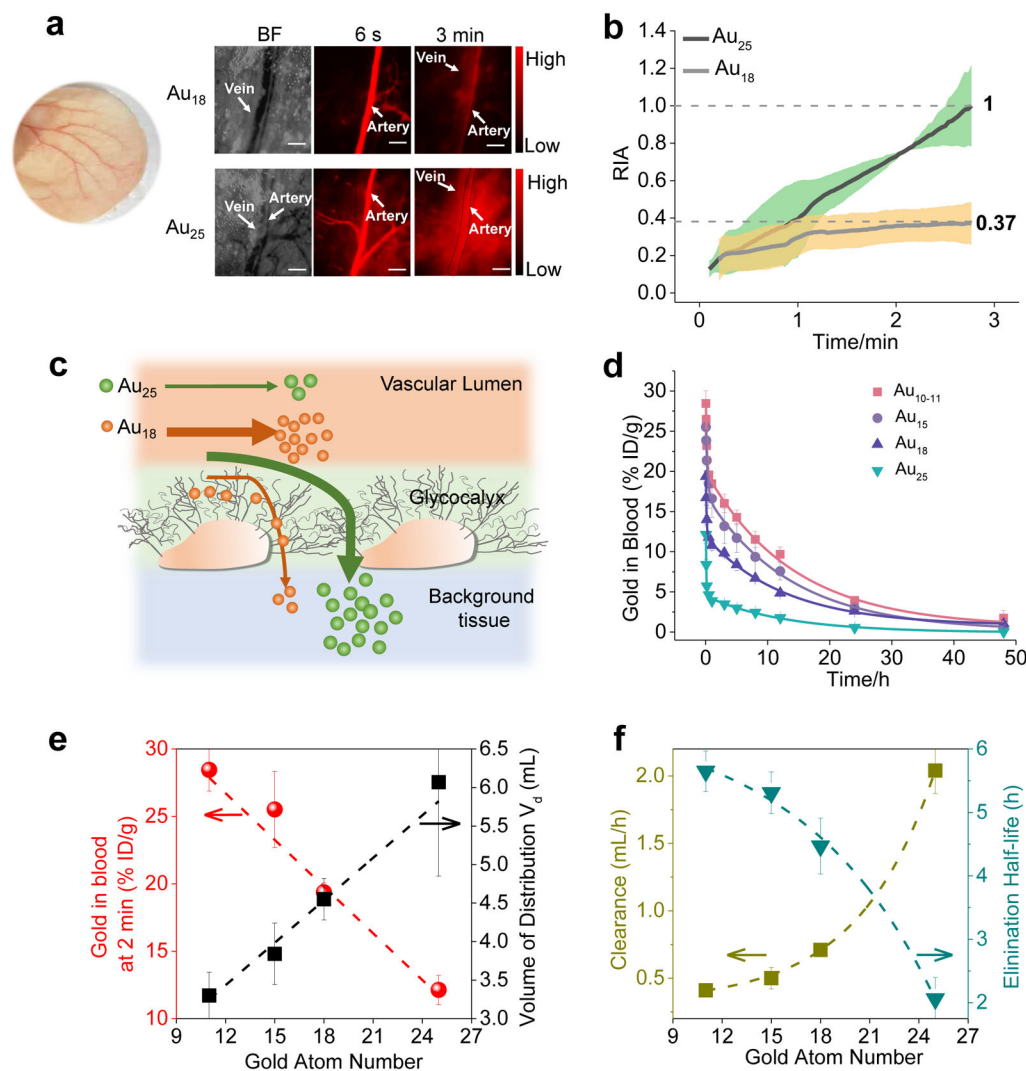
Figure 3. *In vivo* behaviors of few-atom gold nanoclusters

a, Noninvasive bright-field and fluorescence images of mouse ear blood vessels after intravenous injection of Au_{18} and Au_{25} at 6 s and 3 min, respectively, showing that Au_{25} crossed the endothelium more rapidly than Au_{18}. Scale bar: 150 μm. BF: bright field. Color picture of mouse ear was inserted. **b**, The ratio of (interstitial intensity-background intensity)/(artery intensity- background intensity) (RIA) of Au_{18} and Au_{25}, gray shadow represents standard deviation from different mouse (n=3 per group). This result showed that Au_{25} is much more permeable than Au_{18}. **c**, Schematic diagram of Au_{18} and Au_{25} crossing blood vessel walls. The junction between endothelial cells is about 5 nm. The smaller Au_{18} has higher affinity with the glycocalyx of the endothelium of the blood vessels than Au_{25}; as a result, few of Au_{18} was extravasated into interstitial space of tissues than Au_{25} during the same time period. **d**, Blood pharmacokinetics of Au_{10-11}, Au_{15}, Au_{18} and Au_{25}. Although all the clusters show two-compartment pharmacokinetics, they exhibit distinct distribution and elimination half-lives even though there are only few-atom differences among these clusters (n=3, mean ± s.d.). **e,** Correlation of the number of gold atoms in the clusters with

their retention in the plasma at 2 min. p.i., and their volume distribution (Vd) derived from pharmacokinetics measurements, showing that the blood retention was linearly decreased but the Vd of AuNCs linearly increased with the increase of the number of gold atoms. **f**, Correlation of elimination half-life and clearance (CL) of few-atom AuNCs with the number of gold atoms, showing that clearance exponentially increases but elimination half-life exponentially decreased with the increase of the number of gold atoms in the clusters.
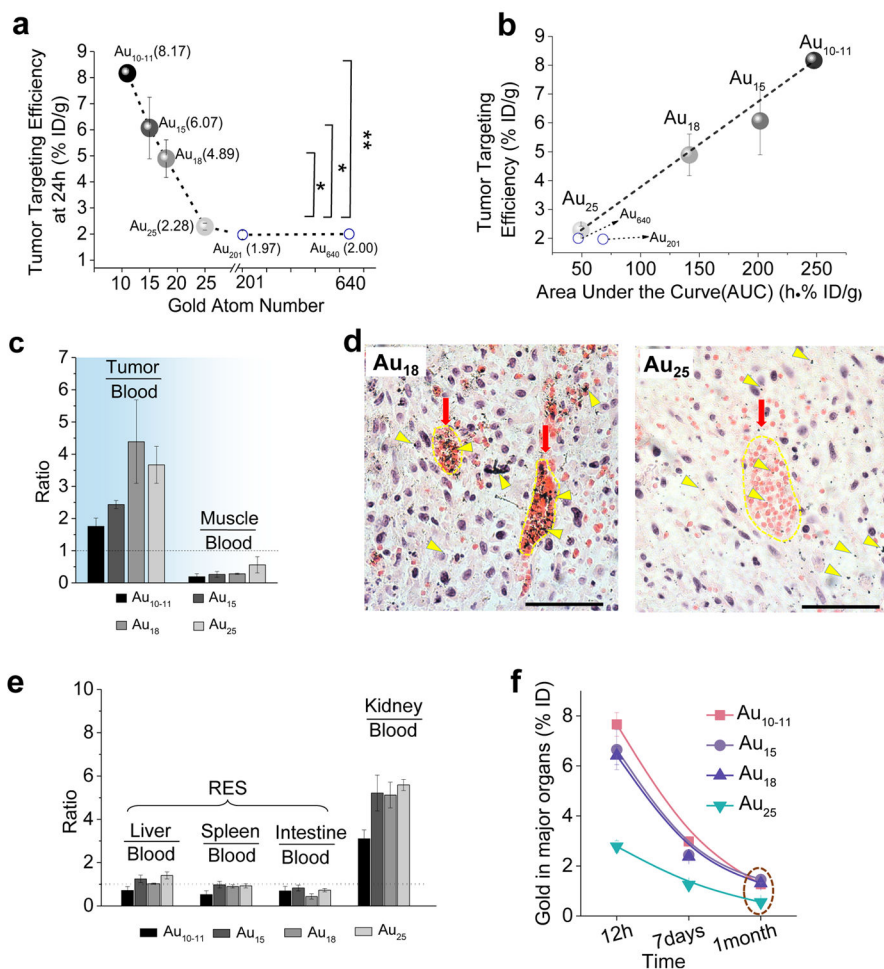
Figure 4. Tumour targeting efficiency and long-term accumulation in body

a, The relationship between tumour accumulation efficiency of Au_{10-11}, Au_{15}, Au_{18} and Au_{25} (n=3, mean ± s.d.) and ~1.7 nm AuNPs (Au_{201}) and ~2.5 nm AuNPs (Au_{640}) at 24 h post injection (p.i.). Below Au_{25}, tumour targeting efficiency increased with the decrease of the number of gold atoms. Above Au_{25}, tumour targeting efficiency are comparable. * P<0.05, ** P<0.005, Student's t-test. **b**, The linear relationship between tumour targeting efficiencies 24 h p.i. and area under the pharmacokinetics curve (AUC) (n=3, mean ± s.d.), indicating that the tumour targeting of these AuNCs originated from EPR effect. **c,** Ratios of tumour/blood and muscle/blood of Au_{10-11}, Au_{15}, Au_{18} and Au_{25} at 24 h p.i. (n=3, mean ± s.d.). These tumour/blood ratios of all the sub-nm AuNCs are all larger than 1 and much higher than muscle/blood ratios, showing that the selective accumulation of sub-nm AuNCs in tumour is fundamentally due to enhanced permeability and retention (EPR) effect. **d,** The distribution of Au_{18} and Au_{25} in MCF-7 tumour at 24 h p.i. Major tumour vasculatures were indicated with red arrows. Silver-stained Au_{18} and Au_{25} were indicated with yellow triangles. Nucleus and cytoplasm were stained by H&E. Scale bar is 50 μm. These images clearly showed that more Au_{18} were accumulated in tumour microenvironment and vasculatures than Au_{25}. **e,** Ratios of liver/blood, spleen/blood, intestine/blood and kidney/blood for Au_{10-11}, Au_{15}, Au_{18} and Au_{25} at 24 h p.i (n=3, mean ± s.d.). **f,** The accumulation

of Au_{10-11}, Au_{15}, Au_{18} and Au_{25} in the major organs in the body includes: brain, stomach, intestine, heart, spleen, lung, liver and kidney at 12 h, 7 days and 1 month p.i. (n=3, mean ± s.d.).